Kovove Mater. 60 2022 327–340
DOI: 10.31577/km.2022.5.327

Stress corrosion cracking behavior of an as-extruded Mg-1.8Zn-0.5Zr-1.5Gd magnesium alloy in a simulated body fluid

Huai Yao[1,2]*, Xiaoqin Zha[3], Yi Xiong[1,2], Shubo Wang[4], Marko Huttula[1,4], Wei Cao[4]

[1] *School of Materials Science and Engineering, Henan University of Science and Technology, Luoyang Henan 471023, P. R. China*
[2] *Collaborative Innovation Center of Nonferrous Metals of Henan Province, Luoyang Henan 471023, P. R. China*
[3] *Luoyang Ship Material Research Institute, Luoyang 471000, Henan, P. R. China*
[4] *Nano and Molecular Systems Research Unit, Centre for Advanced Steels Research, University of Oulu, FI-90014, Finland*

Abstract

The microstructure, corrosion resistance, and stress corrosion cracking behavior of an as-cast and solid-solution Mg-1.8Zn-0.5Zr-1.5Gd biomagnesium alloy after extrusion deformation were studied. Results show that when the extrusion ratio was 7.7 and the extrusion temperatures were 350 and 360 °C, the as-cast and solid-solution alloys underwent complete dynamic recrystallization, and the grains were significantly refined. The precipitated phase in the extruded alloy is mainly composed of a nano-scale $(Mg, Zn)_3Gd$ and an Mg_2Zn_{11} phase. A small amount of undissolved and broken micron-sized $(Mg, Zn)_3Gd$ phase particles appeared in the as-cast extruded alloy. The electrochemical corrosion produced during the stress corrosion process peeled off the $(Mg, Zn)_3Gd$ phase particles and induced rapid dissolution of the adjacent matrix. As a result, stresses were accumulated, and stress corrosion sensitivity occurred. At the same time, some larger-sized cracks appeared in the tensile fracture of the alloy. The difference in grain size and orientation in different regions of the solid-solution extruded alloy leads corrosion fracture to be composed of parallel grooves in different directions. Solution treatment of the magnesium alloy was found to reduce the stress corrosion susceptibility of extruded magnesium alloy and make it promising as a biodegradable implanting material.

K e y w o r d s: magnesium alloy, extrusion, microstructure, stress corrosion cracking

1. Introduction

Among modern implant materials such as stainless steel, titanium alloy, and cobalt alloy, magnesium alloy owns the closest mechanical properties to human bones regarding the density (1.7–2.4 g cm^{-3}) and elastic modulus (41–45 GPa). At the same time, it also has good biocompatibility and degradability, and its degradation products can induce the formation of new bone and promote the healing of damaged bone tissue. Therefore, magnesium alloy has received extensive attention from scientific researchers and has been considered the next-generation medical implant material [1–3]. However, magnesium alloy still faces practical challenges in clinical applications as a typical implant. The degradation rate of medical magnesium alloy in vivo is too fast and prone to local corrosion. Under the action of stress, its degradation rate will be even faster [4]. The excessively fast degradation rate and local corrosion will lead to the loss of the integrity of the graft material's mechanical properties before the tissue heals [5]. At the same time, it easily induces increases in the pH value around the graft material, yet affects the healing of the tissue [6]. For medical magnesium alloy materials used in treating fractures, the mechanical properties must meet the requirements of yield strength (YS) higher than 200 MPa, and elongation (EL) greater than 10 %. For medical magnesium alloy materials for cardiovascular stents, the YS must be higher than 200 MPa, and the EL must be greater than 20 %. Moreover, the corrosion rate should be less than 0.5 mm y^{-1} for the alloy immersed in simulated body fluid (SBF) at 37 °C, and the corrosion should be uniform [7, 8]. Currently, it is difficult for most medical magnesium alloys to meet all these performance requirements simultaneously.

*Corresponding author: e-mail address: yaohuaitougao@126.com

Refining the grain of a magnesium alloy can improve its mechanical properties and corrosion resistance in vivo and achieve uniform corrosion [9]. Extrusion deformation is one of the main methods used to refine the grains of magnesium alloys [10, 11]. The ultimate tensile strength (UTS) and EL of an Mg-2.5Zn--0.7Y-0.7Gd-0.4Zr alloy refined by extrusion deformation increased from 217 MPa and 12.8 % to 278 MPa and 18.7 %, and the corrosion rate decreased from 3.49 to 0.629 mm y^{-1} after the extrusion treatment [12]. The YS and EL of an Mg-4.0Zn-0.5Ca-0.5Ce alloy increased from 125 MPa and 7.5 % to 200 MPa and 27 %, respectively [13]. Moreover, the corrosion rate of an Mg-3.0Gd-2.7Zn-0.4Zr-0.1Mn alloy in SBF decreased from 2.36 to 0.461 mm y^{-1} [14]. The mechanical properties and corrosion resistance of an Mg-6.0Gd-1.0Zn--0.4Zr alloy were significantly improved through extrusion deformation, and the UTS, YS, EL, and corrosion rate of the alloy were 252 MPa, 186 MPa, 24.5 %, and 0.34 mm y^{-1}, respectively [15]. These research results showed that the mechanical properties and corrosion resistance of medical magnesium alloys can be effectively improved through extrusion deformation.

Magnesium alloys are prone to localized corrosion in an environment containing chloride ions, and the resulting corrosion pits usually become the origin of crack propagation [16]. Therefore, stress corrosion cracking is prone to occur in magnesium alloy graft materials under both human body fluid corrosion and an external mechanical load, leading to rapid failure of the alloy [17, 18]. When the strain rate was 3.6×10^{-4} s^{-1}, the UTS, YS, and EL of an Mg-4Zn alloy in SBF, compared with these in air, decreased by 10.0, 23.5, and 11.2 %, respectively [19]. When the strain rate was 3.1×10^{-7} s^{-1}, the UTS and EL of an Mg-2.0Zn-1.0Zr alloy in SBF were lower than those in the air by 20.5 and 62.7 %, respectively [20]. When the strain rate was 3.5×10^{-6} s^{-1}, the UTS and EL of an AZ31 alloy in SBF reduced by 8.9 and 75.1 %, respectively, compared with those in the air [21]. These studies found that under stress, localized corrosion leads to a significant decrease in the mechanical properties of the alloy. Therefore, it is necessary to study the stress corrosion cracking behavior of magnesium alloys to justify the long-term suitability of magnesium alloys for biological implants.

Based on the principle of medical magnesium alloy's biological safety and the previous research of the author [22–24], the grains of as-cast and solid-solution Mg-1.8Zn-0.5Zr-1.5Gd alloys were refined by hot extrusion, and the effect of the microstructure on the corrosion resistance of the alloy was characterized. At the same time, a slow strain rate stress corrosion experiment in SBF was used to explore the effect of the microstructure on the stress corrosion cracking behavior of the alloy.

2. Experimental procedure

2.1. Sample preparation

With pure magnesium (99.9 %), pure zinc (99.9 %), Mg-20Gd (wt.%), and Mg-25Zr (wt.%) alloys used as the raw materials, an Mg-1.8Zn-0.5Zr-1.5Gd alloy was melted under the protection of mixed gas (CO_2 + 2%SF_6) in a ZGJL0.01-40-4 intermediate frequency induction furnace [25]. Inductively coupled plasma atomic emission spectroscopy (Optima 8000) was used to test that the actual composition of the molten alloy was Mg-1.84Zn-0.53Zr-1.51Gd (wt.%). The as-cast alloy went through solution treatment at a temperature of 480 ℃ for 6 h, then was cooled in water at 60 ℃. After the as-cast and solid-solution alloys were processed into cylindrical ingots of ø 50 mm × 35 mm, they were extruded into ø 18 mm round rods at temperatures of 350 and 360 ℃, respectively, and the extrusion rate was about 5 mm s^{-1}. The extruded sample was air-cooled, then subjected to a stress-relieving annealing treatment at 200 ℃ for 4 h. The as-cast and solid-solution extruded alloys are referred to as E1.5 and E_s1.5, respectively.

2.2. Characterizations

Each sample was cut parallel to the extrusion direction to observe the microstructure and test the corrosion resistance. A metallographic microscope (OLYMPUS), a scanning electron microscope (SEM--EBSD, JSM-7800F), a transmission electron microscope (TEM-2100), and an attached energy spectrometer (EDAX) were used to observe the microstructure and analyze the organization, fracture morphology, phase structure, and micro-area composition.

A weightless corrosion experiment, a hydrogen evolution corrosion experiment, and an electrochemical experiment were all carried out in SBF at 37 ℃ [26]. The ratio of the surface area of the sample to the volume of SBF was 1 cm^2 : 30 mL in all three experiments, and the sample size was ø 16 mm × 3 mm. During the experiment, to ensure the stability of the SBF, it was refreshed every 8 h. Hydrogen was collected and measured through a funnel and burette covering the test sample, and the amount of hydrogen evolution was recorded [27]. After the experiment, a 20%CrO_3 + 1%$AgNO_3$ solution was used to remove the corrosion products on the alloy's surface, and the mass of the samples before and after corrosion was weighed. Three parallel samples were taken to analyze the results. The formulae used to calculate the weight loss corrosion rate P_w (mm y^{-1}) and the hydrogen evolution corrosion rate P_H (mm y^{-1}) are shown in Eqs. (1) and (2), respectively [28]:

$$P_w = 8.76 \times 10^4 \times \Delta w / \rho A t, \quad (1)$$

$$P_{\mathrm{H}} = 95.36 \times V_{\mathrm{H}}/\rho At, \quad (2)$$

where Δw is the weight loss of the alloy (mg), ρ is the density of the test sample (g cm^{-3}), A is the surface area of the test sample (cm^2), t is the immersion time (h), and V_{H} is the volume of hydrogen collected (mL).

An electrochemical workstation (Autolab PG--STAT128N) was used for the polarization curve test. The experiment used a three-electrode system: the test sample was the working electrode, a graphite sheet was the counter-electrode, and a saturated calomel electrode was the reference electrode. After the sample had been immersed for 1 h, the polarization curve was tested. The test rate was 1 mV s^{-1}, and the scanning range was – 0.25–0.45 ± 0.3 V from the open circuit potential (OCP)

A stress corrosion test with a slow strain rate was used to evaluate the stress corrosion cracking susceptibility of different samples. The samples were prepared according to the GB/T 15970.7-2000 standard and tested on an MFDL-100 strain tensile machine. The tensile direction was parallel to the extrusion direction, the tensile rate was 1×10^{-6} s^{-1} with three parallel samples, and the test environment was room temperature air and 37℃ SBF. The dimensions of a tensile specimen are shown in Fig. 1.

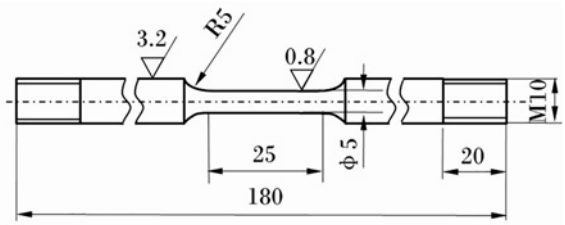

Fig. 1. Size of the tensile sample (mm).

3. Experimental results

3.1. Microstructure

Figure 2 shows the metallurgical organization of the Mg-1.8Zn-0.5Zr-1.5Gd alloy in different states. It can be seen from Fig. 2a that the as-cast alloy is

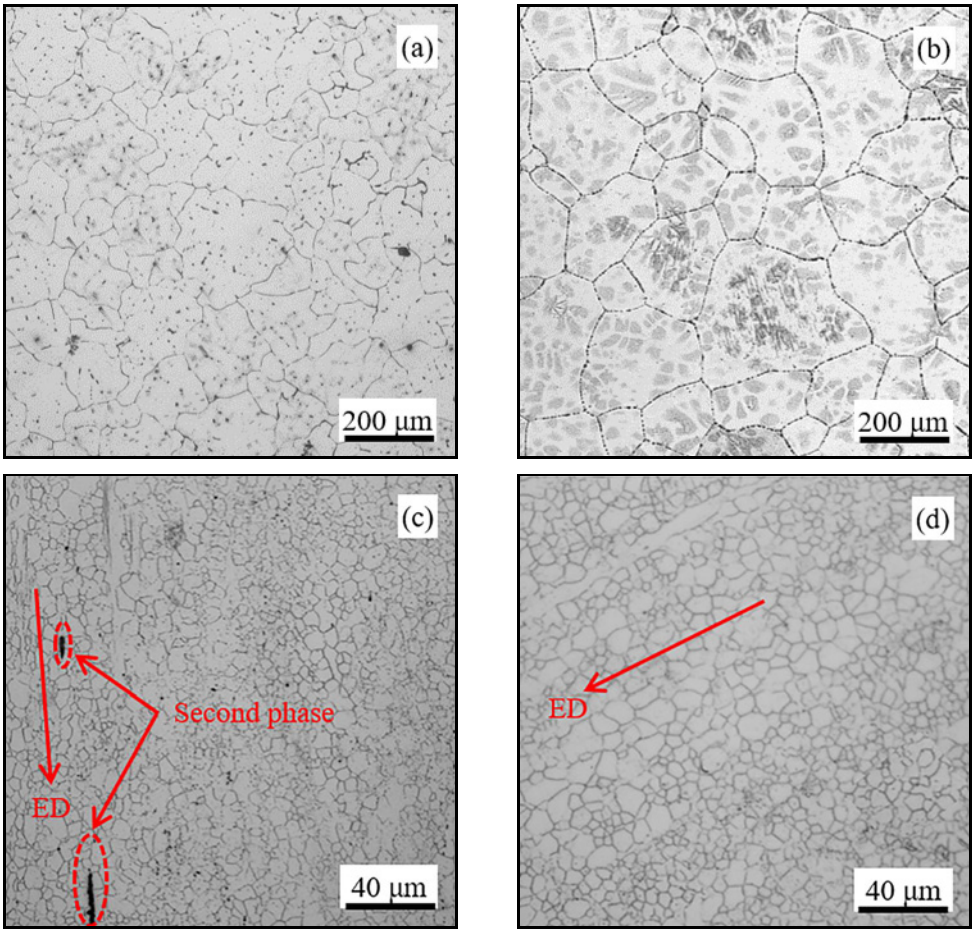

Fig. 2. Optical micrographs of the Mg-1.8Zn-0.5Zr-1.5Gd alloy in different states: (a) as-cast, (b) solid-solution, (c) E1.5, and (d) E$_s$1.5 alloys.

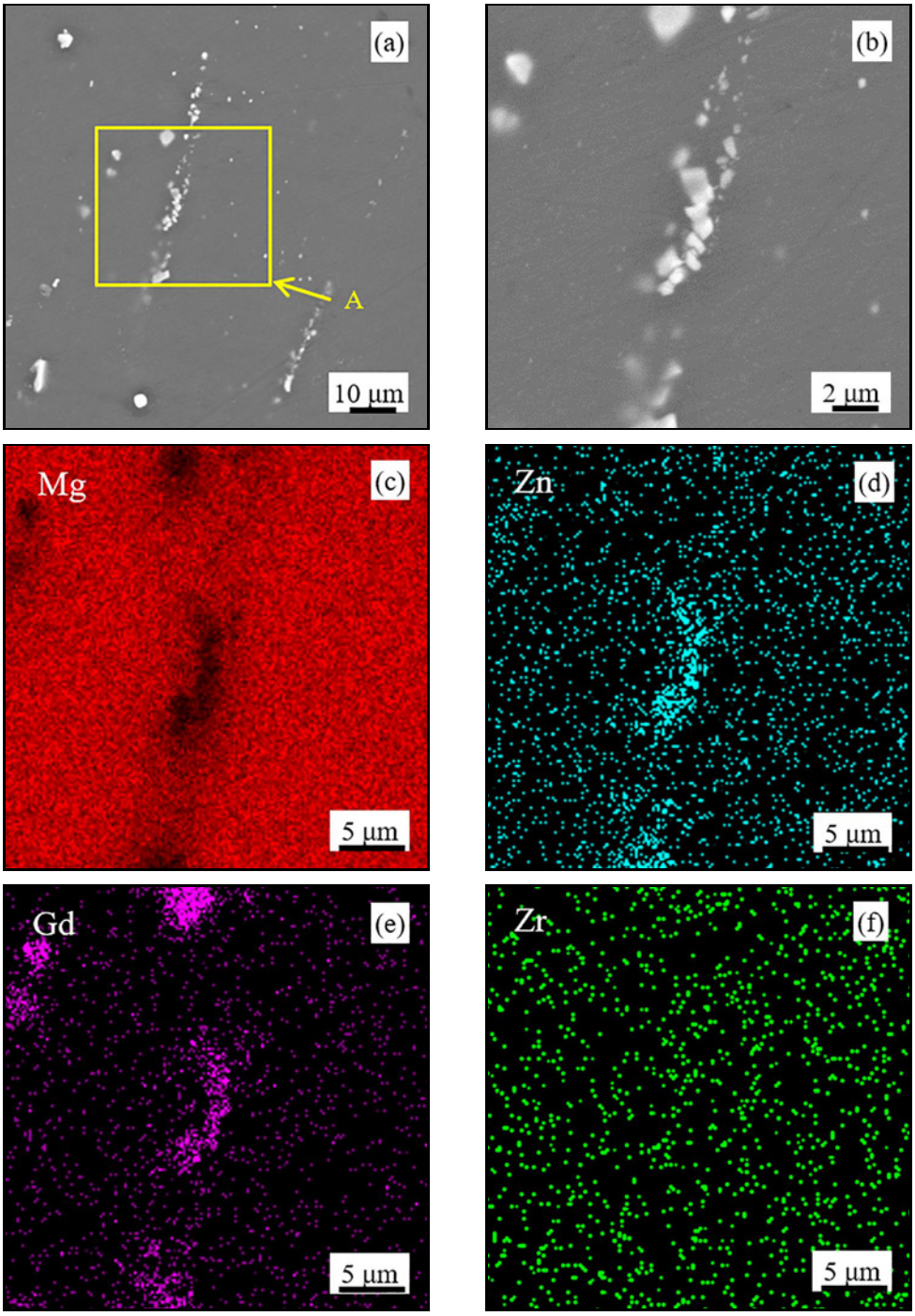

Fig. 3. SEM images in backscattered mode (a), (b), and the corresponding EDX maps (c)–(f) for the E1.5 alloy.

mainly composed of an α-Mg matrix, a black network, and a granular second phase, and the average grain size is about 103 μm. The solid solution alloy has a relatively uniform grain structure, with an average grain size of about 123 μm (Fig. 2b). It can be inferred that the second phase in the original as-cast alloy has dissolved relatively well into the alloy matrix during the solid solution process. In Figs. 2c,d, the grains of the E1.5 and E_s1.5 alloys have been refined. Complete dynamic recrystallization has occurred, and the grain size is about 6.2 μm and 7.3 μm. This indicates that the extrusion temperature and the amount of deformation met the conditions for complete dynamic recrystallization of the alloy. At the same time, small amounts of undissolved second phase particles are distributed in strips in the direction of extrusion in the E1.5 alloy matrix.

Figure 3 shows SEM images of the E1.5 alloy and surface scanning analysis images of Mg, Zn, Gd, and Zr. It can be seen in Fig. 3a that the second phase in

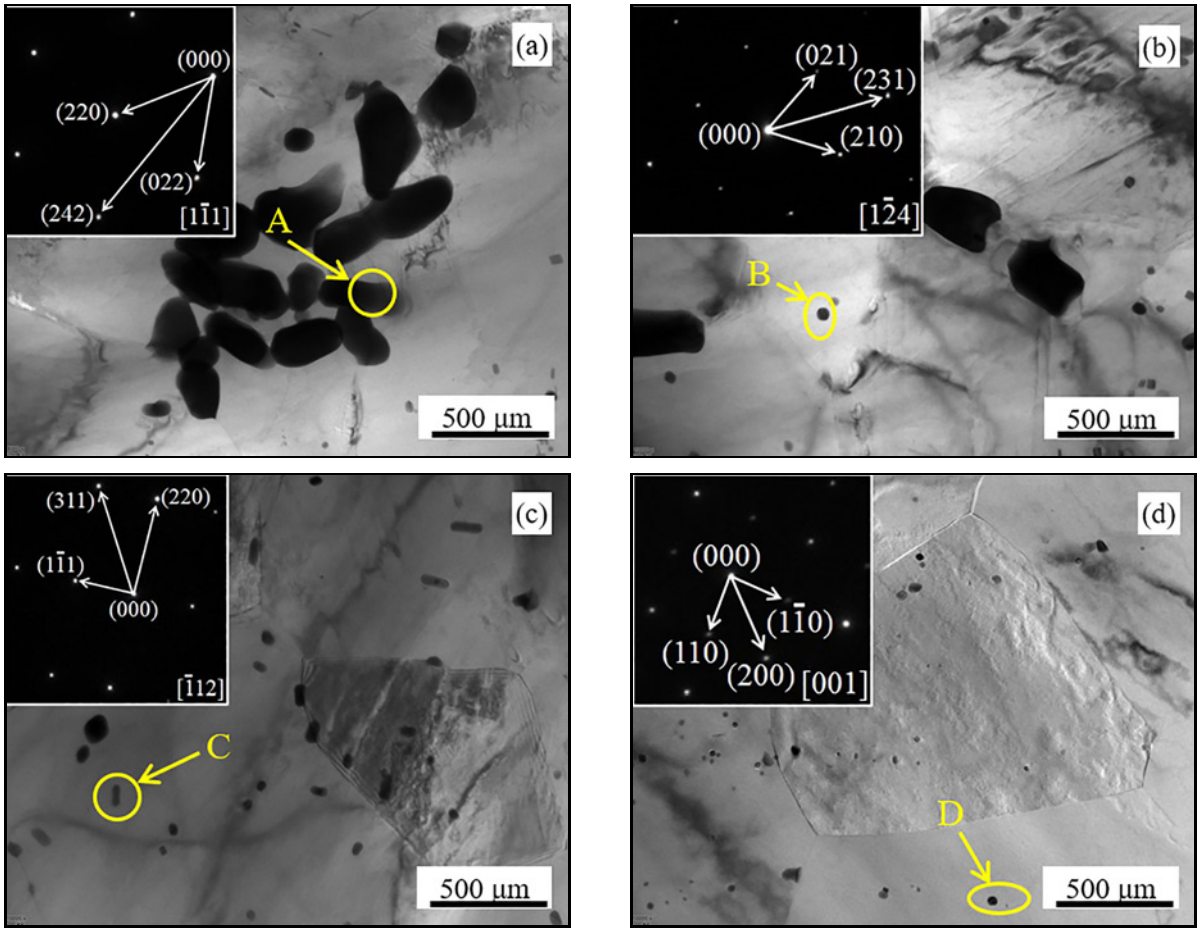

Fig. 4. TEM images and corresponding SAED patterns of (a), (b) the E1.5 alloy, and (c), (d) the E_s1.5 alloy.

the alloy is mainly distributed in the form of particles or strips along the direction of extrusion. Figure 3b shows an enlarged image of Area A in Fig. 3a and Figs. 3c–f show the distribution of the elements Mg, Zn, Gd, and Zr in Fig. 3b. It can be seen in Figs. 3c–f that the second phase in the E1.5 alloy is mainly composed of three elements: Mg, Zn, and Gd, and the Zr is uniformly distributed in the alloy.

Figure 4 shows transmission electron microscopy (TEM) images and selected area electron diffraction (SAED) spots of the E1.5 and E_s1.5 alloys. In Figs. 4a,b, the second phase in the E1.5 alloy is mainly composed of densely distributed micron-sized broken second-phase particles and nano-scale precipitated phase particles with a diverse distribution. The micron-level second-phase particles in Area A in Fig. 4a were calibrated by SAED. The second-phase particles had a face-centered cubic structure. The interplanar distances of the SAED spots are 0.2578, 0.1484, and 0.2578 nm, which correspond well to the (220), (242), and (022) crystal planes of the standard Mg_3Gd phase. At the same time, the second-phase particles are mainly composed of Mg, Zn, and Gd (Table 1). Therefore, it was inferred that the micron-sized second-phase particles are the $(Mg, Zn)_3Gd$ phase. SAED spot calibration of the nano-scale spherical precipitated phase particles in Area B (Fig. 4b) showed that the precipitated phase particles had a cubic crystal structure, and the interplanar distances of the SAED spots were 0.3814, 0.2278, and 0.3815 nm. The interplanar distances correspond well with the (021), (231), and (210) crystal planes in the standard Mg_2Zn_{11} phase. At the same time, the nano-scale spherical precipitated phase particles are mainly composed of Mg and Zn (Table 1). Therefore, it was inferred that the nano-scale precipitated phase particles

Table 1. EDS analyses of the second phases with different morphologies marked in Fig. 4

Position	Mass fraction (%)			
	Mg	Zn	Gd	Zr
A	55.68	17.14	27.18	0
B	98.34	1.66	0	0
C	70.83	12.44	16.73	0
D	98.62	1.38	0	0

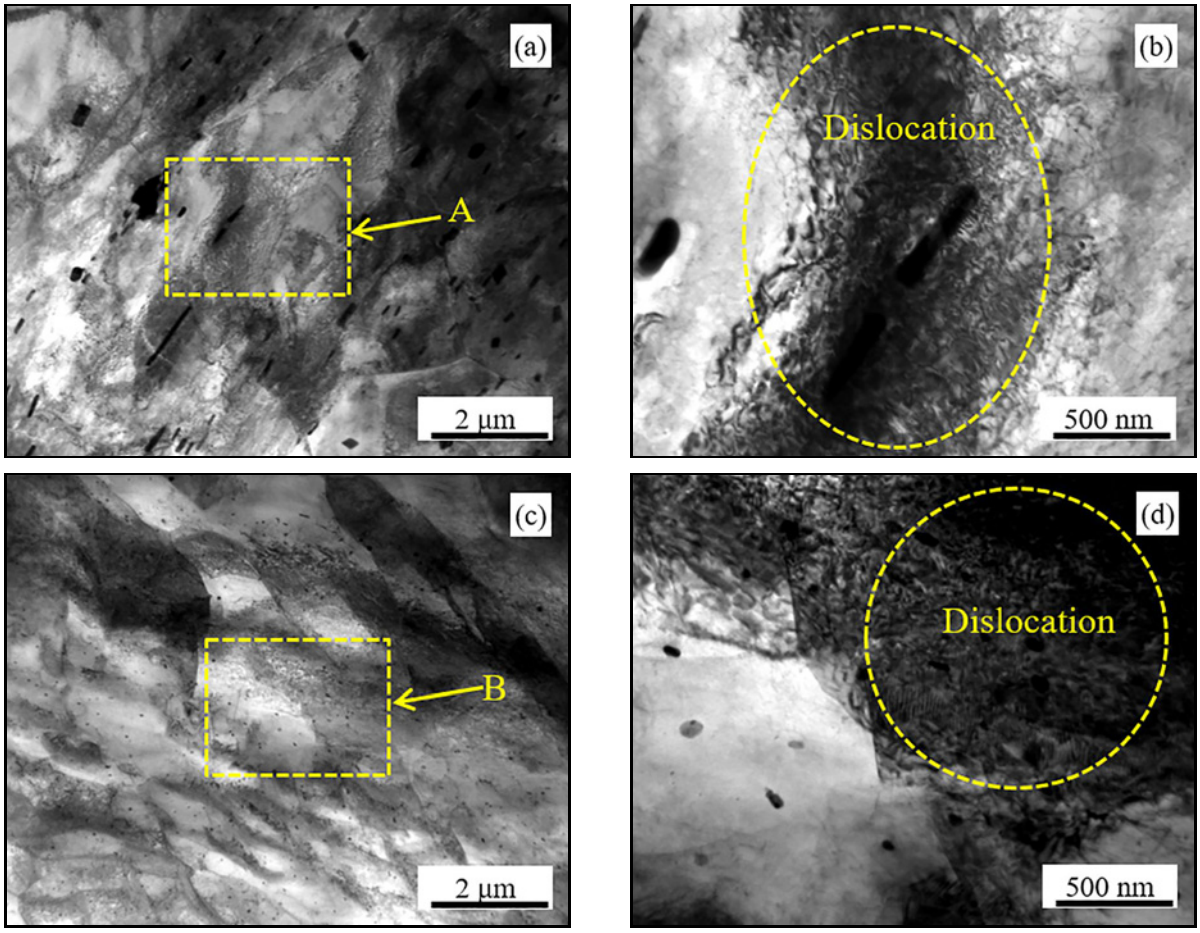

Fig. 5. TEM images of the E1.5 and E_s1.5 alloys: (a) and (b) E1.5; (c) and (d) E_s1.5.

belong to the Mg_2Zn_{11} phase. Similar $(Mg, Zn)_3Gd$ phases and Mg_2Zn_{11} phases are also found in other Mg-Zn-Zr-Gd alloys [29, 30].

In Figs. 4c,d, the second phase in the E_s1.5 alloy is mainly composed of dispersed nano-scale rod-shaped precipitated phase particles and nano-scale spherical precipitated phase particles. SAED spot calibration was performed on the nano-scale rod-shaped precipitated phase particles in Area C in Fig. 4c. The nano-scale rod-shaped particles have a face-centered cubic structure. The interplanar distances are 0.2579, 0.2199, and 0.4218 nm, which corresponds to the (220), (311), and $(11\bar{1})$ crystal planes. The nano-scale rod-shaped precipitated phase particles are mainly composed of Mg, Zn, and Gd (Table 1). Therefore, it was inferred that the nano-scale rod-shaped second-phase particles belong to the $(Mg, Zn)_3Gd$ phase. SAED spot calibration of the nano-scale spherical precipitated phase particles in Area D in Fig. 4d was carried out. The nano-scale spherical precipitated phase particles have a simple cubic structure. The interplanar spacing of the SAED spots is 0.6041, 0.4272, and 0.6041 nm, which corresponds well with the (110), (200), and $(1\bar{1}0)$ crystal planes of standard Mg_2Zn_{11}. The nano-scale spherical precipitated phase particles are mainly composed of Mg and Zn (Table 1). Therefore, it was inferred that the nano-scale spherical precipitated phase particles belong to the Mg_2Zn_{11} phase.

Figure 5 shows a TEM image of the E1.5 and E_s1.5 alloys after the stress corrosion test in SBF. In Figs. 5a,c, after the stress corrosion test, there were a large number of dislocations of different densities in the matrix of the E1.5 and E_s1.5 alloys. Figures 5b,d show partly enlarged images of Areas A and B in Fig. 5a and Fig. 5c, respectively. It can be seen in Figs. 5b,d that there are high-density dislocation plugging products in local areas of the E1.5 and E_s1.5 alloys after the stress corrosion test. The stress corrosion test of the E1.5 and E_s1.5 alloys considered the plastic deformation behavior of each alloy at room temperature. When the deformation temperature is low, dense dislocation accumulation will form in the magnesium alloy's structure, and the alloy relies only on the dislocation slip of the base surface to coordinate the entire plastic deformation process [31]. As the amount of deformation increases, the dislocation density continues to proliferate, and the movement and proliferation of dislocations will cause them to tangle with each other

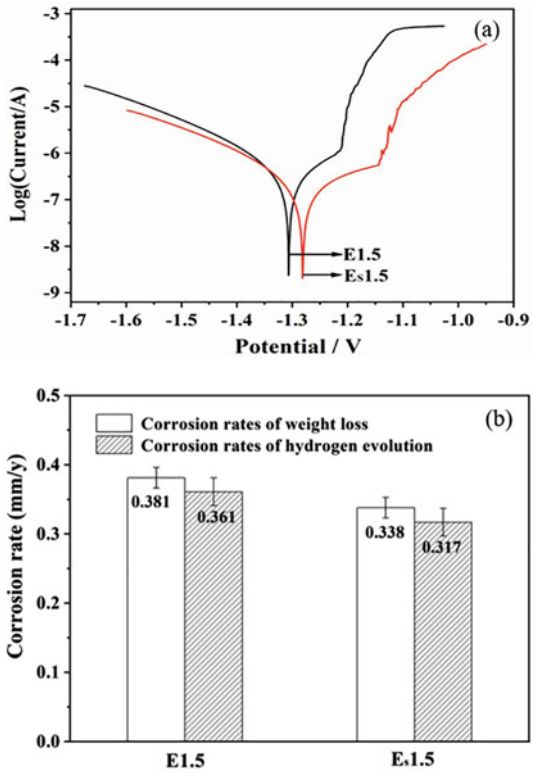

Fig. 6. Polarization curves P_w and P_H for the E1.5 and E_s1.5 alloys.

Table 2. E_{corr}, I_{corr}, and P_i of the E1.5 and E_s1.5 alloys derived from the polarization curves

Material	E_{corr} (Vvs.SCE)	I_{corr} (uA cm^{-2})	P_i (mm y^{-1})
E1.5	–1.306 ± 0.012	2.551 ± 0.014	0.099 ± 0.007
E_s1.5	–1.276 ± 0.013	2.480 ± 0.013	0.086 ± 0.007

during the deformation process to form a high-density dislocation zone [32]. Therefore, after the stress corrosion test, the E1.5 and E_s1.5 alloys had a higher density of dislocations in parts of the microstructure.

3.2. Corrosion resistance

Figure 6 shows the polarization curves of the E1.5 and E_s1.5 alloys after immersion in SBF for 1 h (Fig. 6a) and P_w and P_H in the E1.5 and E_s1.5 alloys after 120 h of immersion (Fig. 6b). Table 2 shows the self-corrosion potential (E_{corr}), the self-corrosion current density (I_{corr}) and the self-corrosion rate (P_i) obtained by Tafel extrapolation from Fig. 6a. In Fig. 6 and Table 2, the E_{corr} of the E_s1.5 alloy was higher, and the values of I_{corr}, P_i, P_w, and P_H were smaller, indicating that the E_s1.5 alloy has better corrosion resistance.

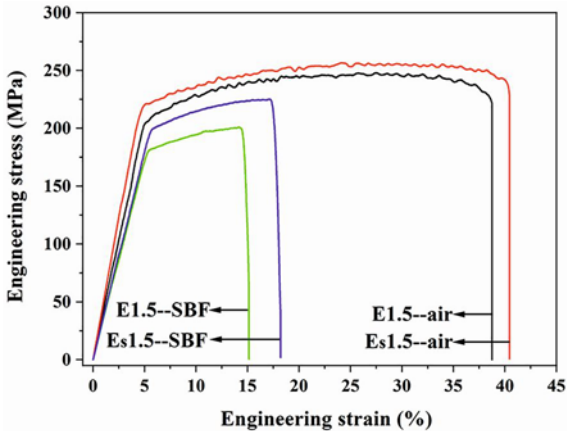

Fig. 7. Engineering stress-strain curves of the E1.5 and E_s1.5 alloys in air and SBF at a strain rate of 1×10^{-6} s^{-1}.

3.3. Slow strain rate tensile testing

Figure 7 shows the slow strain rate tensile stress-strain curves of the E1.5 and E_s1.5 alloy samples in air and SBF. The corresponding UTS, YS, and EL values are shown in Table 3. In air and SBF, the E_s1.5 alloy had better mechanical properties than the E1.5 alloy. Compared with that in air, the UTS, YS, and EL of the E1.5 and E_s1.5 alloys in SBF decreased significantly, those of the E1.5 alloy by 18.9, 24.1, and 60.9 %, and those of the E_s1.5 alloy by 11.9, 9.4, and 54.9 %, respectively. The UTS, YS, and EL of the E1.5 alloy decreased severely, indicating that it is more prone to stress corrosion in SBF.

Figure 8 shows the tensile fracture morphology of the E1.5 and E_s1.5 alloys in the air. Figures 8a,c show the macroscopic morphologies of the tensile fractures

Table 3. Mechanical properties of the E1.5 and E_s1.5 alloys in air and SBF

Material	E1.5 (air)	E_s1.5 (air)	E1.5 (SBF)	E_s1.5 (SBF)
UTS (MPa)	248.4 ± 3.6	256.3 ± 3.5	201.5 ± 3.5	225.6 ± 3.4
YS (MPa)	211.3 ± 3.5	220.2 ± 3.3	160.4 ± 3.2	199.6 ± 3.2
EL (%)	38.7 ± 1.4	40.4 ± 1.3	15.1 ± 1.2	18.2 ± 1.3

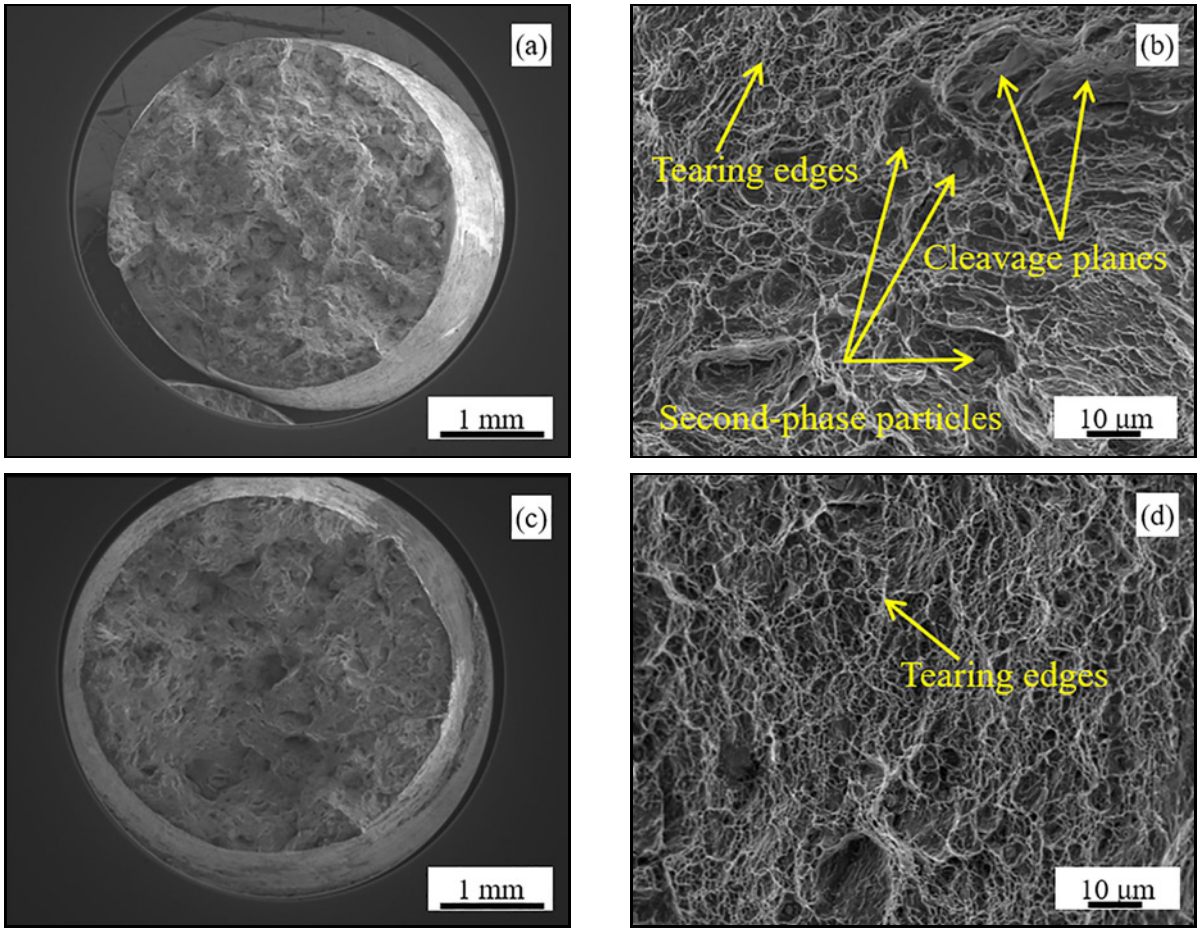

Fig. 8. Fractures of the E1.5 and E_s1.5 alloys at a strain rate of 1×10^{-6} s^{-1} in air.

Table 4. EDS of the surface of the fractures in the E1.5 and E_s1.5 alloys in SBF

Position	Mg	O	C	Zn	Ca	P
B	46.6	42.1	9.4	1.2	0.4	0.3
C	45.3	41.9	10.5	1.5	0.5	0.4

of the E1.5 and E_s1.5 alloys. These are similar in that they both show an apparent necking phenomenon, which corresponds well with the extension process. The microscopic morphologies of the tensile fractures of the E1.5 and E_s1.5 alloys appear similar, as shown in Figs 8b,d. These fractures mainly consist of many dimples, tearing edges, and quasi-cleavage surfaces, showing the typical characteristics of ductile fracture. Compared with the E1.5 alloy, the proportion and size of the dimples in the fractures of the E_s1.5 alloy are larger, and the proportion of quasi-cleavage planes is smaller. As shown in Fig. 8b, there are micron-sized second-phase particles in the central area of some of the dimples in the fractures of the E1.5 alloy.

Figure 9 shows the tensile fracture morphologies of the E1.5 and E_s1.5 alloys in SBF. Figures 9a,d show the macroscopic morphologies of the tensile fractures of the E1.5 and E_s1.5 alloys. Compared with Figs. 8a,c, the necking phenomenon is not apparent, and the fracture is relatively flat, which corresponds well with the reduced elongation. Figures 9b,e show the microscopic morphologies of the tensile fractures of the E1.5 and E_s1.5 alloys without removing the corrosion products. It can be seen from the figures that the fractures are similar, and they are mainly discontinuously corrugated. If we enlarge Areas A and B in Figs. 9b,e, the corrosion products are all in the form of flakes and are perpendicular to the fracture. EDS analysis of Areas A and B in Table 4 shows that the products of corrosion are mainly composed of Mg, O, C, Zn, Ca, and P in different proportions, which are the composition elements of $Mg(OH)_2$, $Ca_{10}(PO_4)(OH)_2$, and $(Ca, Mg)_3(PO4)_2$. After the magnesium alloy was immersed in SBF for a specific time, the corrosion products mainly comprised $Mg(OH)_2$, $Ca_{10}(PO_4)(OH)_2$, and $(Ca, Mg)_3(PO_4)_2$. Generally, the morphology of the corrosion products will vary with soaking time and changes in the corrosion rate [33, 34]. Figures 9c,f show the tensile fracture micromorphologies of the E1.5 and E_s1.5 alloys after removing the corrosion products. As shown in Fig. 9c, the E1.5 alloy had many

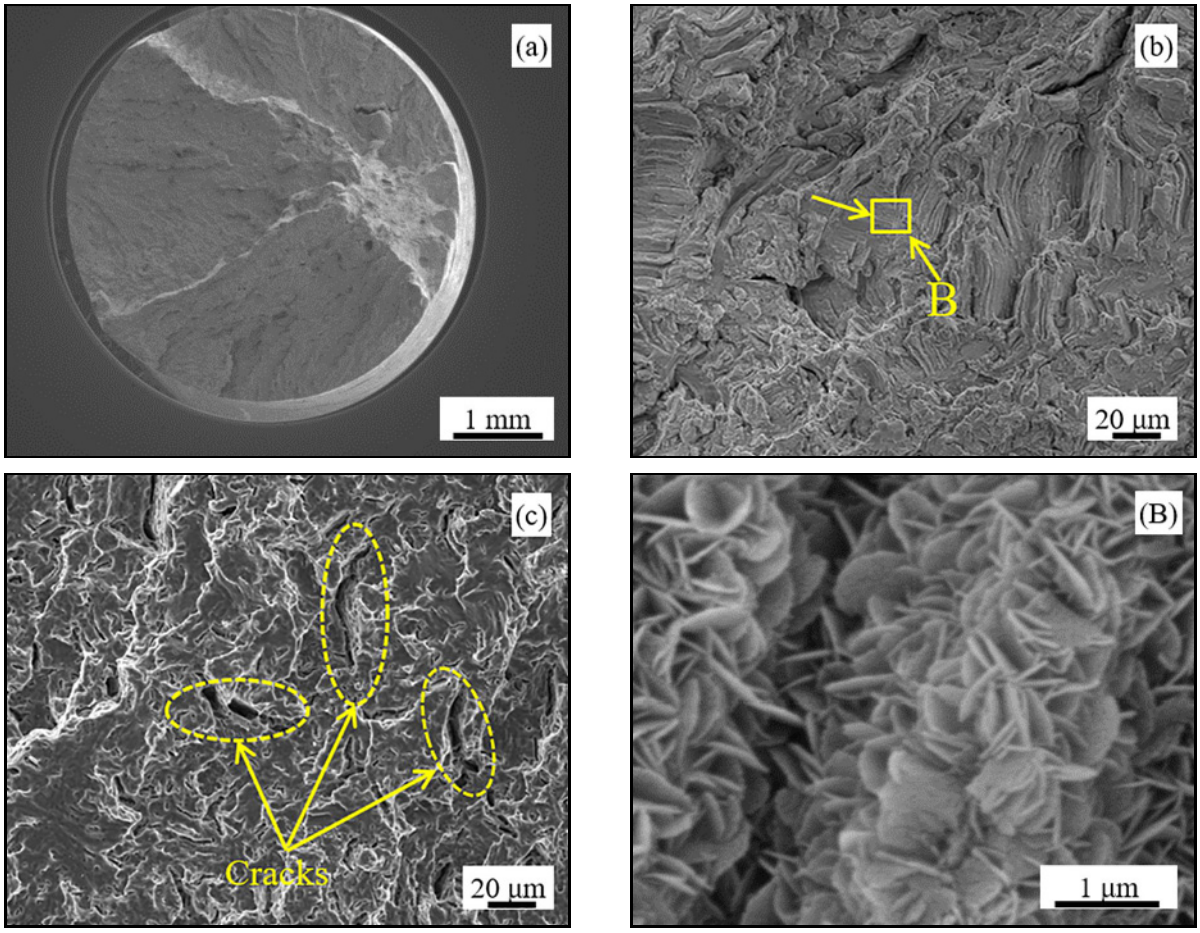

Fig. 9a–c. Fractures of the E1.5 and E_s1.5 alloys at a strain rate of 1×10^{-6} s^{-1} in SBF.

cleavage planes perpendicular to the tensile direction, hydrogen-induced transgranular fracture characteristics in some areas along the cleavage plane [35, 36], and some larger corrosion cracks in the fracture area. It can be seen from Fig. 9f that a large number of parallel groove structures with different orientations appeared in the tensile fracture of the E_s1.5 alloy, and a small number of shallow dimples and microcracks also appeared in the fracture. The E1.5 and E_s1.5 alloys both showed typical brittle fracture characteristics.

4. Discussion

4.1. Microstructure evolution

During the thermoplastic deformation of a magnesium alloy, the stress is mainly concentrated in the grain boundary and the second-phase particle (> 1 μm) region. As a result, the accumulation and density of dislocation in the grain boundary and the second-phase particle regions increase. The accumulation and increase in dislocation density will promote the nucleation and growth of dynamically recrystallized grains in this area. At the same time, the formation and growth of dynamically recrystallized nuclei will also absorb a certain amount of dislocations and reduce dislocations in the alloy. Decreasing the density of dislocations and releasing the accumulated stress can improve plasticity and facilitate the progress of deformation [37]. As shown in Fig. 2a, a certain number of larger-sized second-phase particles appear in the as-cast Mg-1.8Zn-0.5Zr-1.5Gd alloy. The deformation process can cause dislocations to accumulate, causing, in turn, the alloy to have a greater deformation storage energy, thereby increasing the driving force of recrystallization to promote the further occurrence of dynamic recrystallization. During the process of extrusion deformation, some of the larger second-phase particles in the original as-cast alloy were broken and refined, and dispersed in the alloy matrix. These dispersed second-phase particles (> 1 μm) can promote the occurrence of dynamic recrystallization through particle excitation nucleation [38]. It can also be seen from Fig. 2a that the as-cast alloy has a smaller grain size, indicating that the as-cast alloy contains a larger number of grain boundaries per unit of volume, and that the more dynamic recrystallization nucleation areas that can be provided during the deformation process, the more favorable the dynamic recrystalliza-

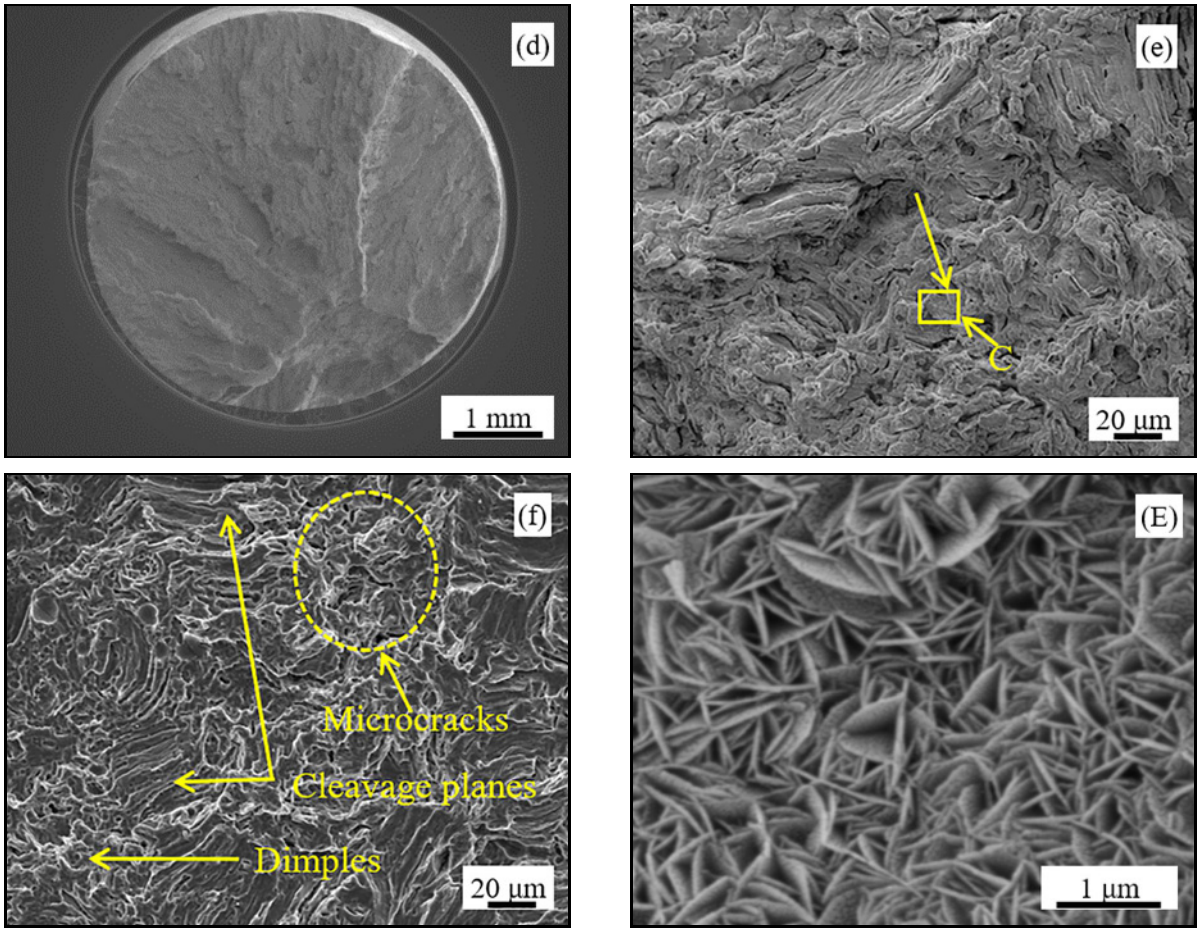

Fig. 9d–f. Fractures of the E1.5 and E_s1.5 alloys at a strain rate of 1×10^{-6} s^{-1} in SBF.

tion [39]. When the solution temperature and time are 480 ℃ and 6 h, respectively, the second phase in the Mg-1.8Zn-0.5Zr-1.5Gd alloy mainly exists in the form of dispersed nano-scale particles [40]. The fine and dispersed second-phase particles usually have a strong pinning effect on the alloy's grain and sub-grain boundaries, hindering their migration, and thus inhibiting the dynamic recrystallization nuclei and the occurrence of dynamic recrystallization [41]. Increasing the extrusion temperature can reduce the activation energy of the migration of atoms in the alloy and drive their rapid diffusion. Besides, increasing the temperature also makes dislocation movement easier and increases the nucleation rate of dynamic recrystallization and the migration ability of grain boundaries, thus promoting the occurrence of dynamic recrystallization [42]. Therefore, it is necessary to increase the extrusion temperature to promote complete dynamic recrystallization of the solid-solution Mg-1.8Zn-0.5Zr--1.5Gd alloy.

It can be seen from Figs. 4c,d that a certain number of nano-scale rod-shaped (Mg, $Zn)_3Gd$ precipitated phase particles and nano-scale elliptical or spherical Mg_2Zn_{11} precipitated phase particles are dispersed in the E_s1.5 alloy. Therefore, it can be inferred that during the solid solution and extrusion process, the alloying elements dissolved better into the alloy matrix, and supersaturated solid solutions formed in some areas. Furthermore, the difference in the amount and atomic radius of Gd and Zn caused differences in the types and morphologies of the nano-scale precipitated phases during the cooling process [43].

4.2. The influence of microstructure on corrosion behavior

The corrosion resistance of Mg-Zn-Zr-Gd alloys in SBF is mainly related to the grain size, the amount of alloying elements dissolved in the matrix, and the second-phase parameters (morphology, size, and volume fraction) [44]. When the size of the alloy's grains is similar, the amount of alloying elements dissolve in the alloy matrix, and the number, size, and volume fraction of the second-phase particles play a leading role in its corrosion resistance [45]. It can be seen from Figs. 2–4 that the E1.5 alloy contains some second-phase particles larger than 1 μm. The second-phase particles usually act as a cathode during the corrosion process, which accelerates the corrosion of the alloy matrix and increases the alloy's corrosion rate

[46]. The E_s1.5 alloy contains a small amount of dispersed nano-scale precipitated phase particles, indicating that extrusion deformation after the solution treatment makes the alloying elements dissolve better and more uniformly into the alloy matrix. The alloy elements dissolved in the matrix increase the E_{corr} of the matrix, reducing the potential difference between the matrix and the second phase. At the same time, the dissolution of a large amount of alloying elements into the matrix also reduces the volume fraction of the cathode phase in the alloy, reduces the power of electrochemical corrosion, and improves the corrosion resistance of the alloy [47]. Therefore, the E_s1.5 alloy has better corrosion resistance than the E1.5 alloy.

4.3. Stress corrosion cracking

From the point of view of dislocation, the smaller the alloy grains, the more grain boundaries and the greater the resistance are needed to overcome the nearby dislocation network when dislocations move during the stretching process. Macroscopically, the strength of the alloy increases with grain refinement. The smaller the grain size, the greater the number of grains per unit of volume, and the stress will be dispersed across more grains during the stretching process, which improves the uniformity of deformation and reduces stress concentration [48]. At the same time, the fine grain boundaries are easy to slide and rotate during plastic deformation, which improves the plasticity of the alloy [49]. Therefore, the E1.5 and E_s1.5 alloys had high strength and elongation in the slow strain rate tensile test in air.

As seen in Figs. 2–4, some large undissolved second-phase particles ($> 1\,\mu m$) are densely distributed along the direction of extrusion in the E1.5 alloy. The second-phase particles usually have a non-coherent interface relationship with the matrix, leading to a weaker atomic bonding force between the second-phase particles and the matrix. Therefore, the interface area between the second-phase particles and the matrix usually becomes the source of crack initiation and propagation channels during the stretching process, reducing the mechanical properties of the alloy [50]. Compared with the E1.5 alloy, more Zn and Gd elements were dissolved in the E_s1.5 alloy. Because of the great differences in the atomic radius and elastic modulus of Zn, Gd, and Mg, they can create a better solid-solution strengthening effect [51]. The dispersed nano-scale precipitated phase particles in the E_s1.5 alloy can play a dominant role in strengthening the second-phase particles [52]. Therefore, the E_s1.5 alloy has better mechanical properties, and the change in the mechanical properties corresponds well with the change in fracture morphology.

In the initial stage of stress corrosion of a magnesium alloy in SBF, a corrosion product film first forms on the surface of the alloy. Larger second-phase particles ($> 1\,\mu m$) appear in E1.5 alloy. Under external stress, the contact area of the larger second-phase particles and the matrix is prone to cracks [49], which leads to cracking of the corrosion product film on the surface of the second-phase particles. The product film ruptures, and the bare metal substrate and surrounding corrosion product film act as an anode and cathode, respectively, in the electrochemical corrosion process, forming a small anode-large cathode system. A large instantaneous current can be generated between the two to accelerate the corrosion of the alloy matrix, which generates pitting and forms the source of cracks [53]. The stress is concentrated at the crack tip, accelerating the dissolution of the alloy matrix in the crack area and propagation of the crack. When the crack expands to a critical size, it will cause the alloy to fracture. At the same time, the larger second-phase particles will accelerate the corrosion of the nearby alloy matrix under the action of micro galvanic corrosion. The hydrogen that is too late to overflow during the corrosion process will be adsorbed on the crack tip and diffuse into the alloy, forming a hydrogen concentration gradient enriched at the crack tip. When the hydrogen concentration exceeds a critical value, a certain hydride will be formed at the crack tip, thus reducing the bonding force between atoms in the crack area and causing hydrogen embrittlement [54]. During the stress corrosion process, shedding of the second-phase particles and dissolution of the nearby alloy matrix will also form larger corrosion pits (Fig. 9c), resulting in stress concentration, intensified corrosion, and, finally, rapid fracture of the sample. Therefore, the larger size of the second-phase particles in the E1.5 alloy is the main factor leading to its higher susceptibility to stress corrosion.

For the E_s1.5 alloy, which has a relatively uniform structure distribution, the dislocations on the slip surface are activated by applying stress, resulting in slip steps. In magnesium alloys, the continuity between the larger crystal grains and the MgO layer and $Mg(OH)_2$ layer on the surface is poor. During the stretching process, the corrosion product film in this area is likely to rupture and accelerate the rapid dissolution of the exposed matrix in this area. Crack tips or corrosion pits then form; at the same time, the newly formed corrosion product film will quickly cover the surface of the exposed substrate, preventing the dissolution process from occurring [55]. However, under the action of external stress, stress will be concentrated in the area of the crack tips and corrosion pits, which can easily cause the newly formed corrosion product film to rupture again. When the corrosion product film ruptures, rapid local dissolution repeatedly occurs, resulting in the formation and propagation of stress corrosion cracks. As shown in Fig. 9f, discon-

tinuous crack propagation during the slow stretching process leads to the appearance of a parallel groove structure, and the difference in grain orientation in different regions leads to differences in the direction of the parallel grooves [56]. Therefore, the region with a larger grain size in the bimodal grain structure of E_s1.5 alloy is the main factor leading to its stress corrosion cracking.

For the E1.5 and E_s1.5 alloys, during the stress corrosion process, a large number of high-density dislocation regions will also be generated in the alloy (Fig. 5). These high-density dislocation regions can provide a channel for the diffusion of corrosion product hydrogen, which will accelerate the occurrence of hydrogen embrittlement [36]. At the same time, the high-density dislocation area usually acts as an anode during the corrosion process, which easily leads to localized corrosion and accelerates the fracturing of the alloy [57]. Therefore, in the stress corrosion experiment, the combined effect of microcracks and localized corrosion caused the mechanical properties of the alloy in SBF to decrease significantly.

5. Conclusions

This work studied the microstructure, corrosion resistance, and stress corrosion cracking behavior of as-cast and solid-solution Mg-1.8Zn-0.5Zr-1.5Gd alloys after hot extrusion. The main conclusions are as follows:

1. Both the E1.5 and E_s1.5 alloys underwent complete dynamic recrystallization. Their microstructure was significantly refined, and the grain sizes reduced from 103 μm and 123 μm before extrusion to 6.2 and 7.3 μm, respectively. The precipitated phases in the E1.5 and E_s1.5 alloys were mainly composed of nanoscale $(Mg, Zn)_3Gd$ and Mg_2Zn_{11} phases. At the same time, some densely distributed broken micron-scale $(Mg, Zn)_3Gd$ phase particles were still distributed in the E1.5 alloy.

2. When the strain rate was $1.0 \times 10^{-6}\,s^{-1}$, compared with that in the air, the UTS, YS, and EL of the E1.5 alloy treated with SBF decreased by 18.9, 24.1, and 60.9 %, and those of the E_s1.5 alloy treated with SBF decreased by 11.9, 9.4, and 54.9 %, respectively. The presence of larger second-phase particles in the E1.5 alloy resulted in a greater susceptibility to stress corrosion.

3. In the E1.5 alloy, the rapid dissolution of the matrix in the area near the micron-sized second-phase particles and the shedding of the second-phase particles led to the presence of large corrosion cracks in the corrosion fractures. In different regions of the E_s1.5 alloy, the difference in grain size and orientation made the directions of the microcracks and their propagation differ during the stress corrosion process, resulting in the corrosion fracture comprising different parallel grooves.

Acknowledgements

This work was financially supported by the Education Department of Henan Province (20A430010), National Natural Science Foundation of China (U1804146, 52111530068), Foreign Experts and Introduction Project of Henan Province (HNGD2020009), and Academy of Finland grant #311934.

References

[1] B. N. Du, Z. Y. Hu, J. L. Wang, L. Y. Sheng, H. Zhao, Y. F. Zheng, T. F. Xi, Effect of extrusion process on the mechanical and in vitro degradation performance of a biomedical Mg-Zn-Y-Nd alloy, Bioact. Mater. 5 (2020) 219–227. https://doi.org/10.1016/j.bioactmat.2020.02.002

[2] X. B. Zhang, G. Y. Yuan, L. Mao, J. L. Niu, P. H. Fu, W. J. Ding, Effects of extrusion and heat treatment on the mechanical properties and biocorrosion behaviors of a Mg-Nd-Zn-Zr alloy, J. Mech. Behav. Biomed. Mater. 7 (2012) 77–86. https://doi.org/10.1016/j.jmbbm.2011.05.026

[3] Y. X. Liu, M. Curioni, Z. Liu, Correlation between electrochemical impedance measurements and corrosion rates of Mg-1Ca alloy in simulated body fluid, Electrochim. Acta 264 (2018) 101–108. https://doi.org/10.1016/j.electacta.2018.01.121

[4] D. X. Liu, S. W. Hu, X. Y. Yin, J. J. Liu, Z. Jia, Q. L. Li, Degradation mechanism of magnesium alloy stent under simulated human micro-stress environment, Mater. Sci. Eng. C 84 (2018) 263–270. https://doi.org/10.1016/j.msec.2017.12.001

[5] M. Peron, J. Torgersen, F. Berto, Mg and its alloys for biomedical applications: Exploring corrosion and its interplay with mechanical failure, Metals 7 (2017) 252. https://doi.org/10.3390/met7070252

[6] E. K. Brooks, S. Der, M. T. Ehrensberger, Corrosion and mechanical performance of AZ91 exposed to simulated inflammatory conditions, Mater. Sci. Eng. C 60 (2016) 427–436. https://doi.org/10.1016/j.msec.2015.11.059

[7] M. Janbozorgi, K. K. Taheri, A. K. Taheri, Microstructural evolution, mechanical properties, and corrosion resistance of a heat-treated Mg alloy for the bio-medical application, J. Magnes. Alloys 7 (2019) 80–89. https://doi.org/10.1016/j.jma.2018.11.002

[8] Z. Z. Gui, J. Y. Zhang, Z. X. Kang, Characterization and properties of Mg-xGd-1.5Nd-0.5Zn-0.5Zr alloys for biodegradation application, Materials 13 (2020) 1421. https://doi.org/10.3390/ma13061421

[9] E. V. Parfenov, O. B. Kulyasova, V. R. Mukaeva, B. Mingo, R. G. Farrakhov, Y. V. Cherneikina, A. Yerokhin, Y. F. Zheng, R. Z. Valiev, Influence of ultra-fine grain structure on corrosion behaviour of biodegradable Mg-1Ca alloy, Corros. Sci. 163 (2020) 108303. https://doi.org/10.1016/j.corsci.2019.108303

[10] J. H. Li, Y. B. Zhang, Y. F. Wang, Q. Zeng, Y. Zhuang, Investigation on microstructure, mechanical properties and work hardening behavior of as-extruded Mg--4.5Zn-0.75Y-xZr alloys, Mater. Res. Express. 6 (2019) 126558. https://doi.org/10.1088/2053-1591/ab57c1
[11] Y. Zhang, X. Y. Chen, Y. L. Lu, X. P. Li, Microstructure and mechanical properties of as-extruded Mg-Sn--Zn-Ca alloy with different extrusion ratios, T. Nonferr. Metal. Soc. 28 (2018) 2190–2198. https://doi.org/10.1016/S1003-6326(18)64864-2
[12] Y. Z. Xu, J. Y. Li, M. F. Qi, J. B. Gu, Y. Zhang, Effect of extrusion on the microstructure and corrosion behaviors of biodegradable Mg-Zn-Y--Gd-Zr alloy, J. Mater. Sci. 55 (2020) 1231–1245. https://doi.org/10.1007/s10853-019-03978-8
[13] M. Golrang, M. Mobasheri, H. Mirzadeh, M. Emamy, Effect of Zn addition on the microstructure and mechanical properties of Mg-0.5Ca-0.5RE magnesium alloy, J. Alloys Compd. 815 (2020) 152380. https://doi.org/10.1016/j.jallcom.2019.152380
[14] Z. Z. Gui, Z. X. Kang, Y. Y. Li, Corrosion mechanism of the as-cast and as-extruded biodegradable Mg--3.0Gd-2.7Zn-0.4Zr-0.1Mn alloys, Mat. Sci. Eng. C 96 (2019) 831–840. https://doi.org/10.1016/j.msec.2018.11.037
[15] X. B. Zhang, J. W. Dai, Q. S. Dong, Z. X. Ba, Y. J. Wu, Corrosion behavior and mechanical degradation of as-extruded Mg-Gd-Zn-Zr alloys for orthopedic application, J. Biomed. Mater. Res. 108 (2019) 698–708. https://doi.org/10.1002/jbm.b.34424
[16] Y. M. Gao, L. Z. Wang, L. H. Li, X. N. Gu, K. Zhang, J. Xia, Y. B. Fan, Effect of stress on corrosion of high--purity magnesium *in vitro* and *in vivo*, Acta Biomater. 83 (2019) 477–486. https://doi.org/10.1016/j.actbio.2018.11.019
[17] S. Jafari, R. K. S. Raman, C. H. J. Davies, J. Hofstetter, P. J. Uggowitzer, J. F. Löffler, Stress corrosion cracking and corrosion fatigue characterisation of MgZn1Ca0.3 (ZX10) in a simulated physiological environment, J. Mech. Behav. Biomed. 65 (2017) 634–643. https://doi.org/10.1016/j.jmbbm.2016.09.033
[18] L. Choudhary, R. K. S. Raman, Magnesium alloys as body implants: Fracture mechanism under dynamic and static loading in a physiological environment, Acta Biomater. 8 (2012) 916–923. https://doi.org/10.1016/j.actbio.2016.07.039
[19] D. B. Prabhu, S. Dhamotharan, G. Sathishkumar, P. Gopalakrishnan, K. R. Ravi, Stress corrosion cracking of biodegradable Mg-4Zn alloy in simulated body fluid at different strain rates – A fractographic investigation, Mater. Sci. Eng. A 730 (2018) 223–231. https://doi.org/10.1016/j.msea.2018.06.002
[20] S. Jafari, P. K. S. Raman, C. H. J. Davies, Stress corrosion cracking of an extruded magnesium alloy (ZK21) in a simulated body fluid, Eng. Fract. Mech. 201 (2018) 47–55. https://doi.org/10.1016/j.engfracmech.2018.09.002
[21] M. Peron, R. Bertolini, A. Ghiotti, J. Torgersen, S. Bruschi, F. Berto, Enhancement of stress corrosion cracking of AZ31 magnesium alloy in simulated body fluid thanks to cryogenic machining, J. Mech. Behav. Biomed. 101 (2020) 103429. https://doi.org/10.1016/j.jmbbm.2019.103429
[22] G. Y. Yuan, J. L. Niu, Research progress of biodegradable magnesium alloys for orthopedic applications, Acta Metall. Sin. 53 (2017) 1169–1180. https://doi.org/10.11900/0412.1961.2017.00247
[23] Y. J. Chen, Z. G. Xu, C. Smith, J. Sankar, Recent advances on the development of magnesium alloys for biodegradable implants, Acta Biomater. 10 (2014) 4561–4573. https://doi.org/10.1016/j.actbio.2014.07.005
[24] H. Yao, J. B. Wen, Y. Xiong, Y. Lu, M. Huttula, Microstructure evolution in Mg-Zn-Zr-Gd biodegradable alloy: The decisive bridge between extrusion temperature and performance, Front. Chem. 6 (2018) 71. https://doi.org/10.3389/fchem.2018.00071
[25] H. Yao, Y. Xiong, Y. Liu, L. Huan, H. N. Shi, Microstructures and properties of Mg-0.5Zr-1.8Zn-xGd bio-magnesium alloys, Rare Metal Mat. Eng. 49 (2020) 4271–4279.
[26] Y. S. Jeong, W. J. Kim, Enhancement of mechanical properties and corrosion resistance of Mg--Ca alloys through microstructural refinement by indirect extrusion, Corros. Sci. 82 (2014) 392–403. https://doi.org/10.1016/j.corsci.2014.01.041
[27] M. C. Zhao, M. Liu, G. L. Song, A. Atrens, Influence of pH and chloride ion concentration on the corrosion of Mg alloy ZE41, Corros. Sci. 50 (2008) 3168–3178. https://doi.org/10.1016/j.corsci.2008.08.023
[28] H. Yao, J. B. Wen, Y. Xiong, Y. Lu, F. Z. Ren, W. Cao, Extrusion temperature impacts on biometallic Mg-2.0Zn-0.5Zr-3.0Gd (wt.%) solid-solution alloy, J. Alloys Compd. 739 (2018) 468–480. https://doi.org/10.1016/j.jallcom.2017.12.225
[29] Z. Z. Gui, Z. X. Kang, Y. Y. Li, Mechanical and corrosion properties of Mg-Gd-Zn-Zr-Mn biodegradable alloy by hot extrusion, J. Alloys Compd. 685 (2016) 222–230. https://doi.org/10.1016/j.jallcom.2016.05.241
[30] A. Srinivasan, Y. Huang, C. L. Mendis, C. Blawert, K. U. Kainer, N. Hort, Investigations on microstructures, mechanical and corrosion properties of Mg-Gd--Zn alloys, Mater. Sci. Eng. A 595 (2014) 224–234. https://doi.org/10.1016/j.msea.2013.12.016
[31] S. Q. Zhu, H. G. Yan, J. H. Chen, Y. Z. Wu, Y. G. Du, X. Z. Liao, Fabrication of Mg-Al-Zn-Mn alloy sheets with homogeneous fine-grained structures using high strain-rate rolling in a wide temperature range, Mater. Sci. Eng. A 559 (2013) 765–772. https://doi.org/10.1016/j.msea.2012.09.022
[32] A. Chapuis, J. H. Driver, Temperature dependence of slip and twinning in plane strain compressed magnesium single crystals, Acta Mater. 59 (2011) 1986–1994. https://doi.org/10.1016/j.actamat.2010.11.064
[33] L. C. Zhang, M. Z. Xu, Y. D. Hu, F. Gao, T. Gong, T. Liu, X. Li, C. J. Pan, Biofunctionization of biodegradable magnesium alloy to improve the in vitro corrosion resistance and biocompatibility, Appl. Surf. Sci. 451 (2018) 20–31. https://doi.org/10.1016/j.apsusc.2018.04.235
[34] X. B. Zhang, Z. X. Ba, Z. Z. Wang, Y. J. Xue, Microstructures and corrosion behavior of biodegradable Mg-6Gd-xZn-0.4Zr alloys with and without long period stacking ordered structure, Corros. Sci. 105 (2016) 68–77. https://doi.org/10.1016/j.corsci.2016.01.004

[35] L. Choudhary, R. K. S. Raman, Mechanical integrity of magnesium alloys in a physiological environment: Slow strain rate testing based study, Eng. Fract. Mech. 103 (2013) 94–102. https://doi.org/10.1016/j.engfracmech.2012.09.016
[36] J. H. Jiang, Q. Y. Xie, M. S. Qiang, A. B. Ma, E. K. Taylor, Y. H. Li, D. Song, J. Q. Chen, Stress corrosion cracking behaviors of RE-containing ME21 magnesium alloy processed by equal-channel angular pressing, J. Rare Earth 37 (2019) 88–94. https://doi.org/10.1016/j.jre.2018.04.015
[37] T. Al-Samman, Modification of texture and microstructure of magnesium alloy extrusions by particle-stimulated recrystallization, Mater. Sci. Eng. A 560 (2013) 561–566. https://doi.org/10.1016/j.msea.2012.09.102
[38] Y. Tian, H. Huang, G. Y. Yuan, W. J. Ding, Microstructure evolution and mechanical properties of quasicrystal-reinforced Mg-Zn-Gd alloy processed by cyclic extrusion and compression, J. Alloys Compd. 626 (2015) 42–48. https://doi.org/10.1016/j.jallcom.2014.11.167
[39] K. Huang, R. E. Logé, A review of dynamic recrystallization phenomena in metallic materials, Mater. Des. 111 (2016) 548–574. https://doi.org/10.1016/j.matdes.2016.09.012
[40] H. Yao, Y. Xiong, X. Q. Zha, H. Li, H. N. Shi, Y. Liu, Microstructures, mechanical properties and corrosion behavior of solution-treated Mg-0.5Zr-1.8Zn-xGd biodegradable alloys, Rare Metal Mat. Eng. 50 (2021) 1919–1927.
[41] J. D. Robson, D. T. Henry, B. Davis, Particle effect on recrystallization in magnesium-manganese alloy: Particle-stimulated nucleation, Acta Mater. 57 (2009) 2739–2747. https://doi.org/10.1016/j.actamat.2009.02.032
[42] C. J. Li, H. F. Sun, X. W. Li, J. L. Zhang, W. B. Fang, Z. Y. Tan, Microstructure, texture and mechanical properties of Mg-3.0Zn-0.2Ca alloys fabricated by extrusion at various temperatures, J. Alloys Compd. 652 (2015) 122–131. https://doi.org/10.1016/j.jallcom.2015.08.215
[43] H. Yao, H. Li, Y. Liu, H. N. Shi, Enhanced mechanical and corrosion properties of grain refined Mg-2.0Zn--0.5Zr-3.0Gd alloy, Kovove Mater. 58 (2020) 409–421. https://doi.org/10.4149/km_2020_6_409
[44] S. Q. Yin, W. C. Duan, W. H. Liu, L. Wu, J. M. Yu, Z. L. Zhao, M. Liu, P. Wang, J. Z. Cui, Z. Q. Zhang, Influence of specific second phases on corrosion behaviors of Mg-Zn-Gd-Zr alloys, Corros. Sci. 166 (2020) 108419. https://doi.org/10.1016/j.corsci.2019.108419
[45] F. F. Cao, K. K. Deng, K. B. Nie, J. W. Kang, H. Y. Niu, Microstructure and corrosion properties of Mg-4Zn-2Gd-0.5Ca alloy influenced by multidirectional forging, J. Alloys Compd. 770 (2019) 1208–1220. https://doi.org/10.1016/j.jallcom.2018.08.191
[46] Y. F. Ding, C. Wen, P. Hodgson, Y. C. Li, Effects of alloying elements on the corrosion behavior and biocompatibility of biodegradable magnesium alloys: A review, J. Mater. Chem. B 2 (2014) 1912–1933. https://doi.org/10.1039/c3tb21746a
[47] G. Song, A. Atrens, Understanding magnesium corrosion – A framework for improved alloy performance, Adv. Eng. Mater. 5 (2003) 837–858. https://doi.org/10.1002/adem.200310405
[48] M. Mabuchi, K. Kubota, K. Higashi, New recycling process by extrusion for machined chips of AZ91 magnesium and mechanical properties of extruded bars, Mater. Trans. JIM 36 (1995) 1249–1254. https://doi.org/10.2320/matertrans1989.36.1249
[49] H. Y. Yu, H. G. Yan, J. H. Chen, B. Su, Y. Zheng, Y. J. Shen, Z. J. Ma, Effects of minor Gd addition on microstructures and mechanical properties of the high strain-rate rolled Mg-Zn-Zr alloys, J. Alloys Comp. 586 (2014) 757–765. https://doi.org/10.1016/j.jallcom.2013.10.005
[50] D. H. Bae, S. H. Kim, D. H. Kim, W. T. Kim, Deformation behavior of Mg-Zn-Y alloys reinforced by icosahedral quasicrystalline particles, Acta Mater. 50 (2002) 2343–2356. https://doi.org/10.1016/S1359-6454(02)00067-8
[51] S. J. Liu, G. Y. Yang, S. F. Luo, W. Q. Jie, Microstructure and mechanical properties of sand mold cast Mg--4.58Zn-2.6Gd-0.18Zr magnesium alloy after different heat treatments, J. Alloys Comp. 644 (2015) 846–853. https://doi.org/10.1016/j.jallcom.2015.05.062
[52] Y. F. Liu, X. G. Qiao, Z. T. Li, Z. H. Xia, M. Y. Zheng, Effect of nano-precipitation on thermal conductivity and mechanical properties of Mg-2Mn-xLa alloys during hot extrusion, J. Alloys Comp. 830 (2020) 154570. https://doi.org/10.1016/j.jallcom.2020.154570
[53] B. S. Padekar, P. K. S. Raman, V. S. Raja, L. Paul, Stress corrosion cracking of a recent rare-earth containing magnesium alloy, EV31A, and a common Al--containing alloy, AZ91E, Corros. Sci. 71 (2013) 1–9. https://doi.org/10.1016/j.corsci.2013.01.001
[54] E. Merson, P. Myagkikh, V. Poluyanov, D. Merson, A. Vinogradov, On the role of hydrogen in stress corrosion cracking of magnesium and its alloys: Gas--analysis study, Mater. Sci. Eng. A 748 (2019) 337–346. https://doi.org/10.1016/j.msea.2019.01.107
[55] D. B. Prabhu, J. Nampoothiri, V. Elakkiya, R. Narmadha, R. Selvakumar, R. Sivasubramanian, P. Gopalakrishnan, K. R. Ravi, Elucidating the role of microstructural modification on stress corrosion cracking of biodegradable Mg-4Zn alloy in simulated body fluid, Mater. Sci. Eng. C 106 (2020) 110164. https://doi.org/10.1016/j.msec.2019.110164
[56] B. S. Padekar, V. S. Raja, R. K. S. Raman, P. Lyon, Stress corrosion cracking behavior of magnesium alloys EV31A and AZ91E, Mater. Sci. Eng. A 583 (2013) 169–176. https://doi.org/10.1016/j.msea.2013.06.085
[57] M. Andrei, A. Eliezer, P. L. Bonora, E. M. Gutman, DC and AC polarization study on magnesium alloys influence of the mechanical deformation, Mater. Corros. 53 (2002) 455–461. https://doi.org/10.1002/1521-4176(200207)53:7%3C455::AID-MACO455%3E3.0.CO;2-4